Improving access to FORest GENetic resources Information and services for end-Users

Deliverable D3.6

Fitness (fertility estimated by drones, realised fecundity estimated via seedlings modelling) & selection gradients (relationship fitness and trait proxy) for the remaining species.

Planned delivery date (as in DoA): 31/10/2025 (M58)

Actual submission date: 19/12/2025, M60

Workpackage: WP3

Workpackage leader: Delphine Grivet

Deliverable leader: Lars Opgenoorth

Version: 1.0

Project funded by the European Commission within the Horizon 2020 Programme	
Dissemination Level	
PU Public	**X**
CI Classified, as referred to Commission Decision 2001/844/EC	
CO Confidential, only for members of the consortium (including the Commission Services)	

Research and Innovation action: GA no. 862221

Start date of the project: January 1st, 2021

TABLE OF CONTENTS

1 Summary

Deliverable D3.6 establishes a reproducible framework for estimating fertility and realised fecundity in four forest tree species using UAV imagery and genetic neighbourhood modelling. It develops two complementary measures of fitness: (i) an ordinal fertility index derived from reproductive structures visible in the canopy and (ii) realised fecundity inferred from juvenile–adult genetic relationships. (i) A UAV-based workflow was implemented to obtain millimetric-resolution canopy imagery across multiple Genetic Conservation Units (GCUs hereafter). After photogrammetric processing and quality control, two analysis paths were used. High-quality orthomosaics enabled machine-learning classification of reproductive structures and crown-level fertility. In areas where photogrammetric artefacts precluded reliable interpretation, per-tree native-image catalogues were constructed and visually scored using a standardised six-level scheme. Across species and sites, the 0–5 fertility classes captured strong, ordered gradients in reproductive signal, supported by very high Kruskal–Wallis statistics and effect sizes. Fertility classes correlated monotonically with seed signal normalised by basal area, confirming ecological relevance. ML-derived fertility maps showed spatially coherent patterns consistent with stand structure. (ii) Realised fecundity was estimated for *Fagus sylvatica* (beech), *Populus nigra* (black poplar), and *Pinus sylvestris* (Scots pine) using the Bayesian neighbourhood model NMπ. After clone removal (*Populus*) and SNP selection, model parameters for dispersal, mating system and immigration were identified through maximum-likelihood model selection and Bayesian inference. All GCUs exhibited highly skewed fecundity distributions, with a few adults contributing disproportionately to the juvenile cohort. Parentage assignments provided complementary estimates of reproductive success, strongly correlated with realised fecundity. Selection gradients were analysed for Scots pine and beech using the hierarchical neighbourhood model. In Scots pine, no significant gradients were detected in Finland, while turgor loss point showed a positive effect on male fecundity in Britain. In beech, none of the tested hydraulic or structural traits showed significant effects in either GCU. The deliverable provides harmonised, spatially explicit datasets of tree-level fertility, realised fecundity and reproductive success for subsequent modelling of phenotypic and environmental drivers of fitness.

2 Introduction

In situ calibration of selection gradients rests on the estimation of individual fitness. However, local reproductive dynamics are notoriously difficult to estimate under natural conditions due, among other things, to the size and longevity of forest trees, with individual fitness–the reproductive success of an individual–being the most difficult aspect to determine (Petit and Hampe 2006). Therefore, proxies for individual fitness are often used, such as the number of surviving seedlings (realised fecundity) or the number of seeds produced (fertility) by an individual (Avanzi et al. 2020). Fecundity in itself represents a fundamental fitness component that directly influences the evolutionary dynamics of tree populations as individual variation in reproductive output

creates opportunities for selection and affects the allelic frequencies in the next generation (González-Martínez et al. 2006).

Two major ground-based methods being used to estimate seed production from the ground are litter traps and visual counting (Tattoni et al. 2021). These methods are both time-consuming and labour-intensive, as well as often unfeasible in complex terrain, and thus often prohibitive on larger numbers of trees and over several years. Remote sensing technologies hold considerable promise for enabling broad-scale assessments of forest reproductive output, yet satellite-based platforms face fundamental spatial resolution limitations (typically meters to tens of meters) given the spatial scale of reproductive structures (millimetres to centimetres). Unmanned aerial vehicles (UAVs) equipped with high-resolution sensors represent a transformative technology for bridging these resolution gaps. However, we are not aware of studies that have presented a work flow for estimating seed production in forest trees. Thus, the goal of Deliverable D3.6 was to establish a UAV-based pipeline to estimate seed production in forest tree canopies for four species, namely *Fagus sylvatica*, *Populus nigra*, *Pinus sylvestris*, and *Pinus pinaster*.

In addition to developing UAV-based methods for estimating canopy-level fertility, this deliverable quantifies realised fecundity using genetic neighbourhood models (Oddou-Muratorio et al. 2008). Reproductive success in long-lived trees is shaped not only by visible reproductive output but also by the demographic and spatial processes that govern the transition from seed to established seedling. Therefore the fertility estimates are complemented by modelling realised fecundity from adult and juvenile genotypes. Using the Bayesian implementation of the neighbourhood model NMπ (Chybicki 2018, 2023, Chybicki et al. 2021), it is possible to infer the effective contribution of each adult to the next generation while simultaneously estimating dispersal kernels, selfing and immigration rates, and parentage probabilities. This provides a second, independent measure of fitness that integrates processes not detectable from canopy observation alone, such as pollen flow, seed dispersal, and juvenile recruitment. This is further extended by assessing whether particular phenotypic traits act as determinants of reproductive success. Using the hierarchical neighbourhood model in NMπ, trait–fitness associations are evaluated while controlling for confounding demographic and spatial processes that typically bias simple regressions. This approach identifies phenotypic variables whose variation is associated with differences in realised male or female fecundity, thereby providing estimates of selection gradients. Together with the aerial fertility measurements and the realised fecundity estimates, this analysis links reproductive outcomes to functional traits, enabling a more mechanistic understanding of how selection may operate within natural forest stands.

Consequently, we here report how we computed individual-level reproductive success by estimation of seed production from up to 500 adults in each of the eight sites. Estimation of phenotype-fitness relationships were inferred from two approaches: (i) via model-derived realised fecundity estimated in Task 3.1 from genetic data from seedlings and adults (e.g. Oddou-Muratorio et al. 2018); (ii) by using

Unmanned Aerial Vehicles (UAVs) to train remote sensing models to quantify seed production.

3 Results

3.1 Fertility estimated by drones

3.1.1 Drone surveys

We planned low-altitude drone missions to acquire very high-resolution RGB imagery for detecting reproductive structures in the canopy and, thereby, estimating tree-level fertility. These missions were flown with DJI Air 2S, DJI Mavic Pro (×7 optical zoom), and DJI Mavic 3 Multispectral (RGB channel only) in autonomous mode, with the camera in nadir and linear flight lines, maintaining ~10 m AGL above the canopy, ~2 $m \cdot s^{-1}$ cruise speed, and ~85% front/side overlap. This flight geometry, together with the camera optics, set a millimetric Ground Sampling Distance (~1.5–6 mm) and stable sampling for detecting reproductive structures. Camera parameters (exposure time, ISO, trigger rate) were adjusted to illumination to minimize blur, over-/under-exposure, and out-of-focus frames. Ground Control Points (GCPs) visible from multiple angles were installed on the ground and surveyed with GNSS-RTK base–rover (Ultra High Frequency link) at centimeter-level accuracy for photogrammetric georeferencing. The same RTK scheme was used to georeference the ~500 labeled trees per GCU, ensuring 1:1 correspondence between each individual and its visual evidence in the tree catalogs and orthomosaics.

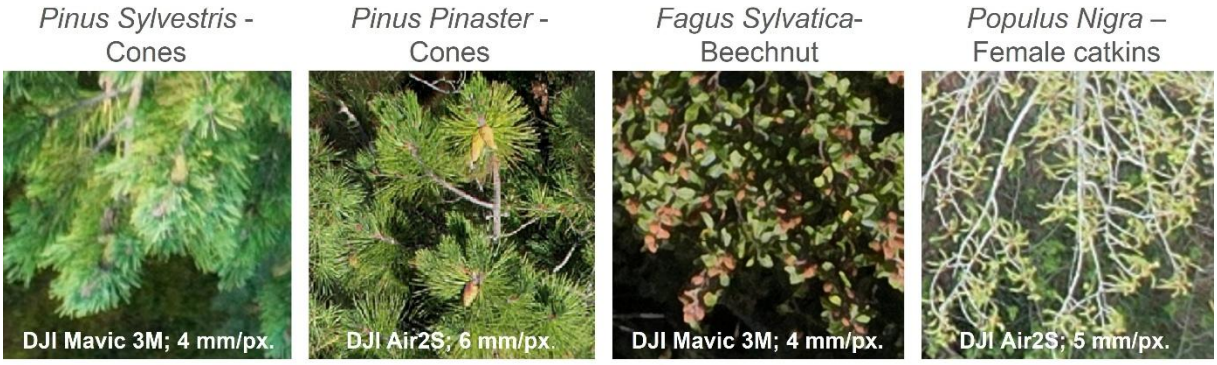

Figure 1. Example UAV RGB close-ups of canopy reproductive structures used for visual QA and fertility scoring: cones of *Pinus sylvestris* and *P. pinaster*, beech nuts of *Fagus sylvatica*, and female catkins of *Populus nigra*, with the corresponding drone platform and ground sampling distance indicated.

3.1.2 Photogrammetric processing

Nadir imagery was processed using Structure-from-Motion in Metashape v1.8.5 (Agisoft LLC), complemented by Ortho+ (Reudenbach, 2023). The workflow comprised: quality control and removal of images with quality < 0.78; an initial alignment via aerial triangulation and bundle block adjustment to obtain a sparse point cloud; a second alignment with stricter parameters integrating georeferenced GCPs; manual marking of each GCP in ≥ 8 images with 70% used as control points and 30% as independent checkpoints; a similarity transformation to refine translation, rotation,

and scale; and iterative optimisation by filtering points using thresholds of Reconstruction Uncertainty (RU ≤ 10), Projection Accuracy (PA ≤ 2), and Reprojection Error (RE ≤ 0.5). The optimised sparse cloud was then used to generate a smoothed 2.5D mesh (TIN interpolation), from which the RGB orthomosaic was produced in the project CRS with uniform scale and minimal distortion.

3.1.2.1 Decision gate: QA-passed orthomosaics vs. per-tree catalogs

We next evaluated orthomosaics against internal QA criteria targeting the semantic readability of seed signals in the canopy. This assessment governs which of two analysis branches is used.

Despite running the full SfM block optimisation with iterative filtering, some orthomosaics still showed artifacts caused by wind-driven canopy motion, illumination variability and shadows, and locally insufficient overlap. Consequently, only **Fig. 2a–c** satisfied the QA requirements for seed-signal semantic readability, with continuous seamlines, low parallax, semi-consistent illumination and stable local GSD. In these high-quality scenes, the RTK-georeferenced adult trees and the training areas used for the Machine Learning (ML) seed-classification approach in panel (**a**) align with the mosaic without offset, the crown annotations in panel (**b**) are coherent, and the seed close-up in panel (**c**) is sharp at the expected scale, confirming both geometric and semantic consistency. By contrast, **Fig. 2d–g** exhibit seam tearing from low overlap, a pronounced shadow wedge, wind-induced parallax with variable light, and local mis-registration. These conditions preclude reliable interpretation on the orthomosaic, so the workflow switches to the per-tree catalog route described next.

Orthomosaics that meet QA proceed to ML-based scoring (**Section 3.1.2.2**). Areas that fail QA are addressed via per-tree catalogs built from native frames and subsequently visually scored (**Section 3.1.2.3**)

3.1.2.2 ML-based scoring on QA-passed orthomosaics

Following the decision gate (**Section 3.1.3**), the ML route is applied exclusively to QA-passed orthomosaics (**Fig. 2a–c**). From these orthomosaics we derive predictor stacks (RGB indices, structural channels, and statistical derivations from Orfeo Toolbox functions extracted from vectors training areas) and train a model following the implementation achieved in Reudenbach et al. (2024) and Mestre-Runge et al. (2025) within the framework of Meyer et al. (2021). Class imbalance is handled by iterative SMOTE tuning, and feature stability by forward selection. Model training/validation enforces spatial independence via leave-cluster-out cross-validation; reliability is then delimited using the Dissimilarity Index (DI) and the Area of Applicability (AOA), which are exported as raster's and propagated in a concise post-classification that also cleans predictions and masks crowns by species rules where required. The output is an ordinal fertility class per tree, aggregated within each RTK-referenced crown geometry and used wherever the orthomosaic meets QA.

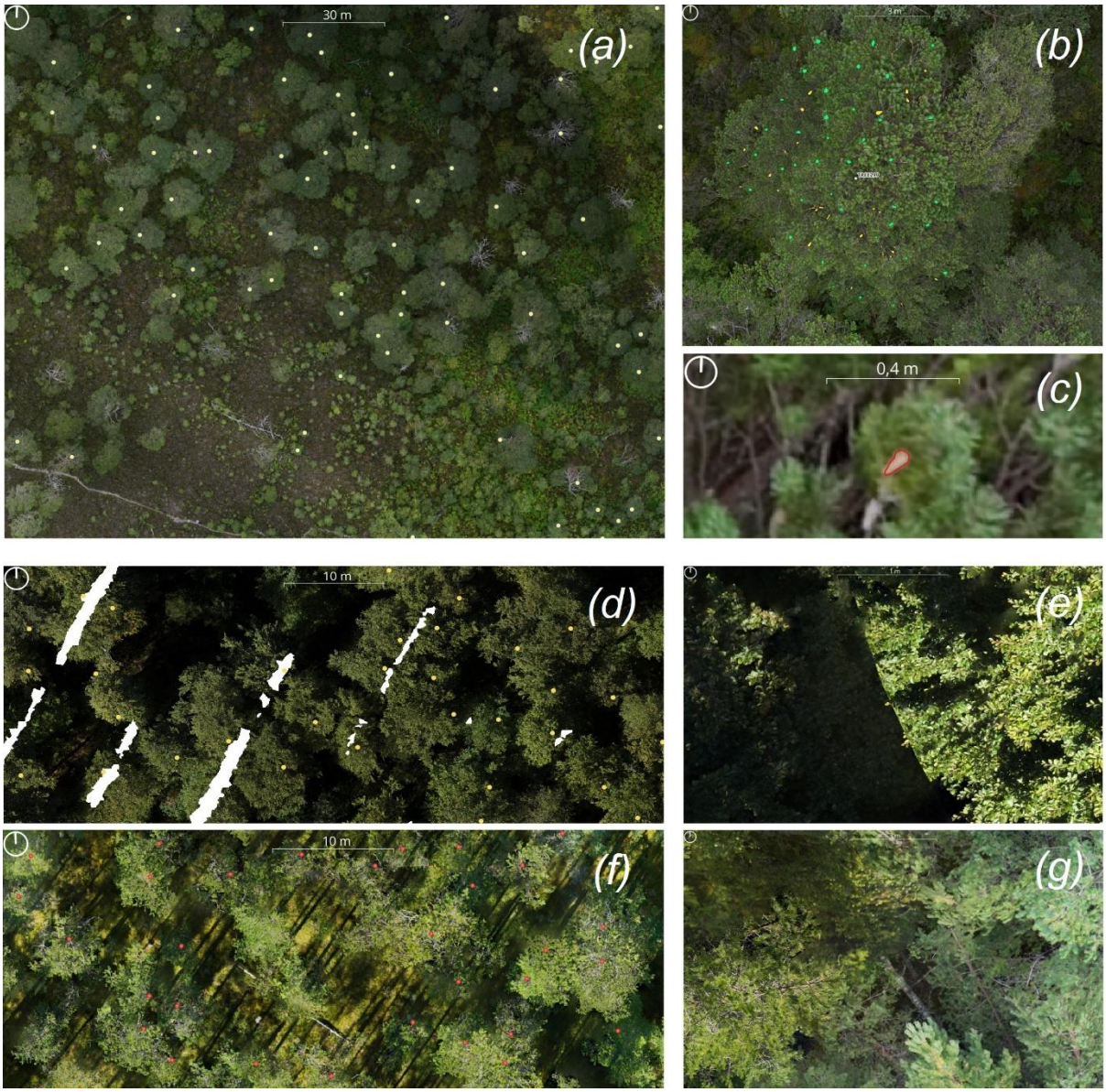

Figure 2. Orthomosaic QA for crown seed-signal interpretation. Panels **(a–c)** meet QA (continuous seamlines, low parallax, consistent illumination/overlap), enabling reliable reading of reproductive-structure semantics. Panels **(d–g)** show artefacts (low-overlap seams, shadowing, wind-induced parallax/ghosting or local mis-registration), so these areas are handled via the per-tree catalog route rather than the orthomosaic.

3.1.2.3 Per-tree catalogs scoring (QA-failed areas)

For those scenes where the QA screening in **Section 3.1.3** identified canopy artefacts likely to bias the semantic reading of reproductive structures, we switched to a per-tree catalog workflow implemented with the *uasimg* tool (Lyons, 2025). Accordingly, we operated directly on native nadir images—preserving pixel resolution and optical sharpness by avoiding photogrammetric resampling—and used each tree's RTK coordinates to (i) locate images whose footprints contain the individual (or the nearest candidates), (ii) rank candidates by tree–image-centre distance to minimise geometric deformation, (iii) retain the best view, and (iv) project it to the project CRS via the *worldfiles* function to establish a one-to-one spatial link with the RTK tree position.

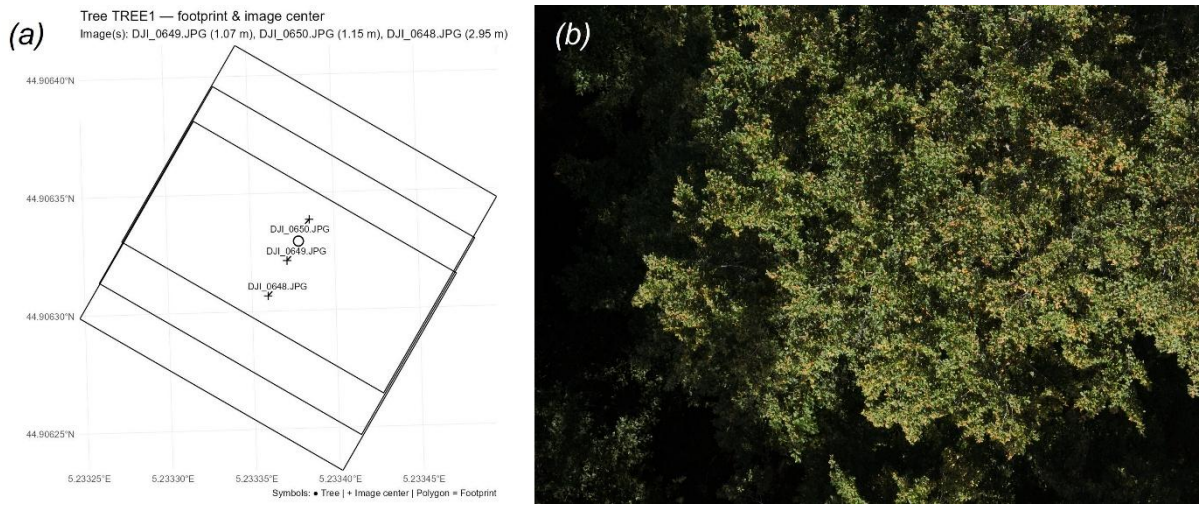

Figure 3. Per-tree catalog via uasimg tool. (a) RTK tree position with footprints and image centres of candidate frames. (b) Retained native-resolution frame georeferenced via world file, used for visual scoring of seed fertility.

Using these per-tree catalogs, each crown is partitioned into four cardinal sectors (N, E, S, W) center on the RTK tree point, and an expert annotator assigns a sector score on a six-level ordinal scale reflecting the visible seed signal (species-specific application per **Table 1**: *Fagus sylvatica* and *Populus nigra* scored by % of sector area with seed signal; *Pinus sylvestris* and *P. pinaster* scored by converting sector-level cone counts to the same 0–5 ordinal scale via project-defined thresholds, ensuring a monotonic, comparable normalisation. For each sector, the annotator reviews the 1–3 available images and records: the ordinal class (0–5), the number of images used (1–3), and optional visibility/occlusion indicators—branch/wood dominance and leaf density (0–5), plus the approximate gap percentage (0–100). A single tree-level class is then derived by aggregating sector scores with a coverage-aware rule: median when ≥3 sectors are available, mean when 2, and NA for <2; the resulting value is mapped back to the same six ordinal labels. Outputs comprise a long table (tree per sector with QA context) and a tree summary (final class, sectors scored, min/max frames used).

This procedure is labour-intensive and inherently subjective because it relies on semantic interpretation of seed evidence in the canopy; nevertheless, it constitutes the visual ground truth against which automated methods are judged. To reduce bias and improve repeatability under a single-annotator protocol, we used prior self-training with species-specific exemplars and periodic self-calibration (refreshing visual references whenever drift was suspected). Consistency was further supported by a standardised scoring template, fixed crown sectoring, explicit visibility/occlusion fields, and a coverage-aware aggregation rule.

Table 1. Ordinal 0–5 sector scale: Fagus/Populus by % area with seed signal; Pinus by cone counts mapped to the same scale (configurable thresholds). Visibility/occlusion guidance applies to all species.

CODE	CLASS LABEL	*FAGUS SYLVATICA* / *POPULUS NIGRA* % OF SECTOR AREA WITH SEED SIGNAL	*PINUS* CONE COUNT (PER SECTOR)	*PINUS* MAPPED CLASS	VISIBILITY / OCCLUSION GUIDANCE *(APPLIES TO BOTH SPECIES)*
0	Absent	0% (no discernible signal)	0	0	If visibility is severely compromised, keep 0 and document QA fields.
1	Very scarce	~1–5%	1–3	1	Use the most conservative class when signals are doubtful.
2	Low	~6–15%	4–10	2	Scattered signals with clear gaps.
3	Medium	~16–35%	11–20	3	Recurrent clusters but not dominant.
4	High	~36–65%	21–40	4	Signal prevalent; limited gaps.
5	Very high	>65%	>40	5 *(upper threshold configurable)*	Near-continuous signal across most of the sector.

3.1.3 Results

As an initial consistency check of the 0–5 ordinal scale, we summarised per-tree reproductive output by species and site and verified that the classes truly order that gradient (**Table 2**). Medians [IQR] locate the typical value and its variability in this campaign: *Fagus sylvatica* 15.5 [0.0] in FRA000045 and 2.0 [0.0] in SVN000047; *P. nigra* 25.0 [25.0] in AUT00284 and 13.5 [13.5] in ESP00395; *P. pinaster* 2.0 [2.0] in FRA000051 and ITA00019; *P. sylvestris* 5.0 [5.0] in FIN000001 and 2.0 [2.0] in GRB000047. An IQR of 0.0 means the central 50% of trees share the same value in that GCU at this phenological snapshot, i.e., low dispersion at this moment. Using a 5% significance threshold, the Kruskal–Walli's test shows very strong differences among classes at all sites (e.g., $H = 196.00$; $p = 2.72\times10^{-41}$ in FSY–FRA000045; $H = 231.00$; $p = 6.53\times10^{-48}$ in PNI–ESP00395). The H statistic increases when between-class differences are large relative to within-class variability; with six classes, values near 200 indicate very pronounced separation produced by the 0–5 scale. Consistently, the effect-size epsilon-squared (ε^2) is very high across sites (0.978–0.994): values near 1 mean that differences among classes explain most of the variation in the quantitative scoring metric within each GCU. Hence, knowing the class lets us anticipate the counted signal level with high precision.

The ecological reading depends on species type. In *Fagus* and *Populus*, the 0–5 class derives from the percentage of crown area showing seed signal; high Kruskal–Wallis together with high ε^2 supports construct validity: as crown area with signal increases, the number of visible units also increases. In *Pi. sylvestris* and *P. pinaster*, the class is derived from raw cone counts mapped to thresholds, so the extremely small *p-values* and $\varepsilon^2 \approx 1$ reflect internal consistency of that mapping—the class effectively codifies the count—rather than additional causal information. Taken together, these metrics indicate where average fertility is higher or lower (medians), how much within-GCU heterogeneity exists (IQR), and how strongly the ordinal scale captures the underlying

quantitative gradient (Kruskal–Wallis and ε^2), providing a comparable ecological readout of per-tree fertility across species and sites for this campaign.

Table 2. Summary by species × GCU for the 0–5 fertility scale. N = trees. Median [IQR] of the quantitative signal used for scoring (percent crown area with seed signal for *Fagus/Populus*; cone counts for Pinus). Kruskal–Wallis H, p test differences among classes; ε^2 is effect size (variance share explained by class). Very small *p* and high ε^2 indicate strong ordering by the 0–5 classes.

Species	*GCU*	*N*	*Median [IQR]*	*Kruskal–Wallis H*	*Kruskal–Wallis p*	*Epsilon squared (ε^2)*
FSY	FRA000045	197	15.50 [0.00]	196.00	2.72×10^{-41}	0.980
FSY	SVN000047	200	2.00 [0.00]	199.00	6.94×10^{-43}	0.985
PNI	AUT00284	253	7.00 [25.00]	252.00	2.05×10^{-52}	0.980
PNI	ESP00395	232	7.00 [13.50]	231.00	6.53×10^{-48}	0.978
PPI	FRA00051	421	0.00 [2.00]	420.00	1.03×10^{-90}	0.993
PPI	ITA00019	370	0.00 [2.00]	369.00	1.15×10^{-79}	0.992
PSY	FIN000001	467	7.00 [5.00]	466.00	1.51×10^{-99}	0.991
PSY	GRB000047	503	2.00 [2.00]	502.00	$<1\times10^{-99}$	0.994

Class profiles (0–5) (**Fig. 4**) by species per site provide a comparable proxy of per-tree fertility within each GCU. In *F. sylvatica*, FRA000045 concentrates in classes 2–3 (stronger seed signal) whereas SVN000047 shifts toward 1 (weaker signal). In *P. nigra*, AUT00284 centers on 3 and ESP00395 on 2, indicating site-level differences in reproductive output. *P. pinaster* is dominated by 0–1 at FRA000051 and ITA00019, i.e., many individuals with absent/very scarce cone signal in the surveyed season. For *P. sylvestris*, FIN000001 groups in 2–3 and GRB000047 in 1–2 with a tail to 3–4, showing moderate output and within-site heterogeneity. Bars report the percentage of trees per class; whiskers are Wilson 95% confidence intervals—narrow where the pattern is precise/consistent, wider where variability or sample size is larger. Overall, these class gradients offer a concise ecological readout of current reproductive output.

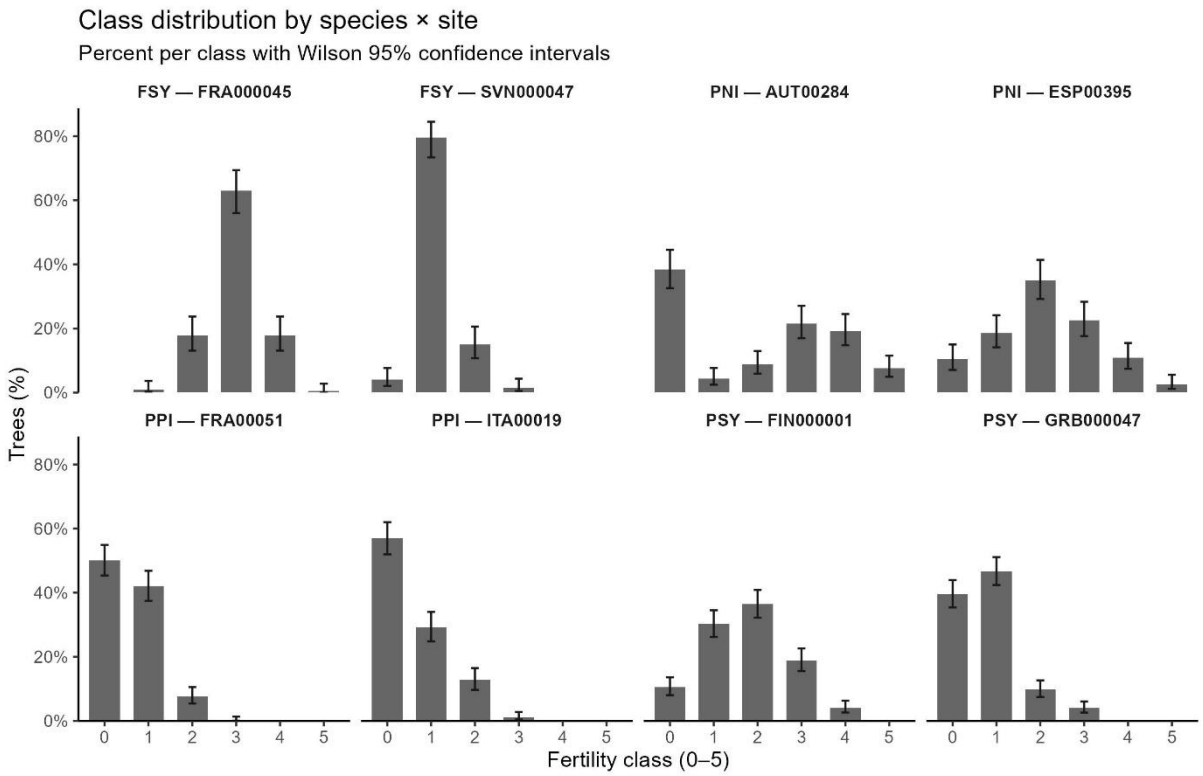

Figure 4. Fertility class distribution (0–5) by species × site. Bars give the percentage of trees per class within each GCU; whiskers are Wilson 95% confidence intervals. Classes summarize the per-tree seed signal (proxy of fertility), allowing direct comparison across species and sites.

The relationship between the 0–5 fertility classes and the seed signal normalised by structure (seeds per basal area) was analysed in two GCUs per species. The fertility class summarises the visual intensity of the reproductive event at crown level, whereas normalisation by basal area controls for tree size (DBH), making comparisons structurally fair. We report Spearman correlations (ρ), which are suitable for assessing monotonic gradients without assuming linearity or normality (**Fig. 5**). Overall, the signal increases monotonically with class and the associations are strong: in *F. sylvatica*, increasing fertility is reflected in an almost stepwise gradient with low within-class variability in both GCUs (ρ = 0.739 in FRA000045; ρ = 0.699 in SVN000047); in *P.s nigra*, the gradient is even sharper and spans the full 0–5 range, with clearly separated medians and moderate dispersion (ρ = 0.908 in AUT00284; ρ = 0.760 in ESP00395); in *P. pinaster*, the response is concentrated in the lower–medium part of the scale, preserving class ordering but with higher dispersion in FRA000051 than in the more compact pattern of ITA00019 (ρ = 0.928; ρ = 0.983); and in *P. sylvestris*, the signal increases consistently from “very scarce” to “high”, without reaching class “very-high, over a relatively compressed range of values (ρ = 0.792 in FIN000001; ρ = 0.881 in GRB000047). The within-species pattern is consistent across sites—similar qualitative slope, different range—and across species, *Populus* and *Pinus* show the most regular relationships, while *Fagus* retains the trend with more contained variation in this campaign. In summary, higher fertility classes imply a higher seed signal per unit of structure, and the strength of the gradient varies in an interpretable way by species and GCU.

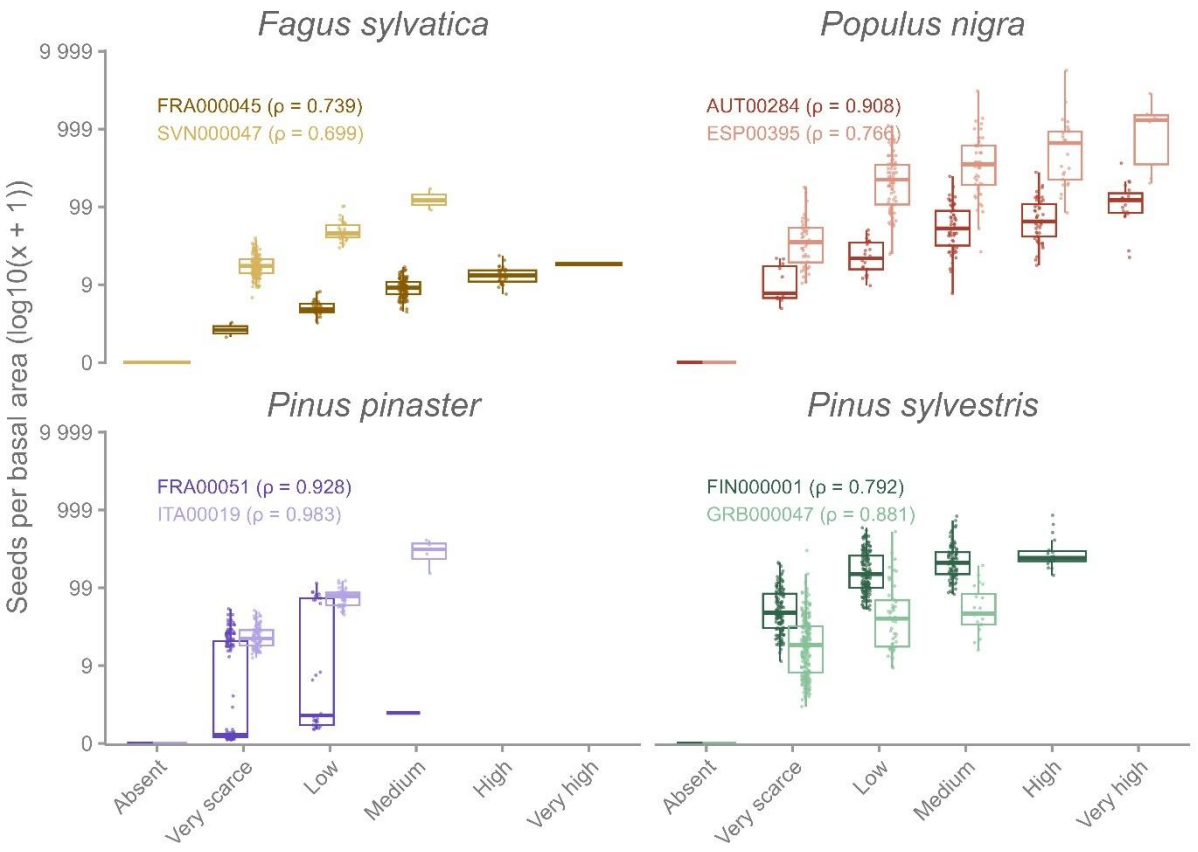

Figure 5. Relationship between fertility classes (0–5) and seed production normalised by structure (log10[seeds per basal area + 1]) for two GCUs per species. Panels show species, colours distinguish GCUs, and boxplots summarise the distribution of individual-tree values (points) within each class. Spearman correlation coefficients (ρ) are reported for each GCU, indicating largely monotonic increases in normalised seed output with increasing fertility class

Seed-fertility maps derived from the ML route illustrate how crown-level predictions can be propagated to the stand scale (**Fig. 6**). At the finest scale, the classifier separates wood, leaves and reproductive structures within individual crowns, generating spatially coherent patches that match the visual patterns in the orthomosaic. Aggregating these pixel-level predictions within each RTK-referenced tree crown yields the 0–5 fertility classes previously analysed, while simultaneously providing a continuous map of seed-bearing canopy elements across the GCU. At the stand scale, the resulting fertility surface reveals structured spatial gradients rather than noisy, isolated detections, suggesting that the model captures biologically plausible patterns of reproduction.

Model performance supports the use of these maps as a basis for spatial analyses. Overall accuracy and agreement metrics are high, and the confusion matrix shows that most misclassifications occur between adjacent or semantically similar classes, with few gross errors. This implies that local uncertainties are mainly class-neighbour swaps rather than spurious artefacts, which is critical when the maps are later used to derive crown-level fertility and to explore spatial structure. Although a formal analysis of spatial autocorrelation and its links to environmental covariates (e.g. topography, topographic wetness index, incoming radiation) is beyond the scope of this report, the

maps provide the necessary multi-scale representation—from individual crowns to the whole GCU—needed to address those questions in a statistically robust way.

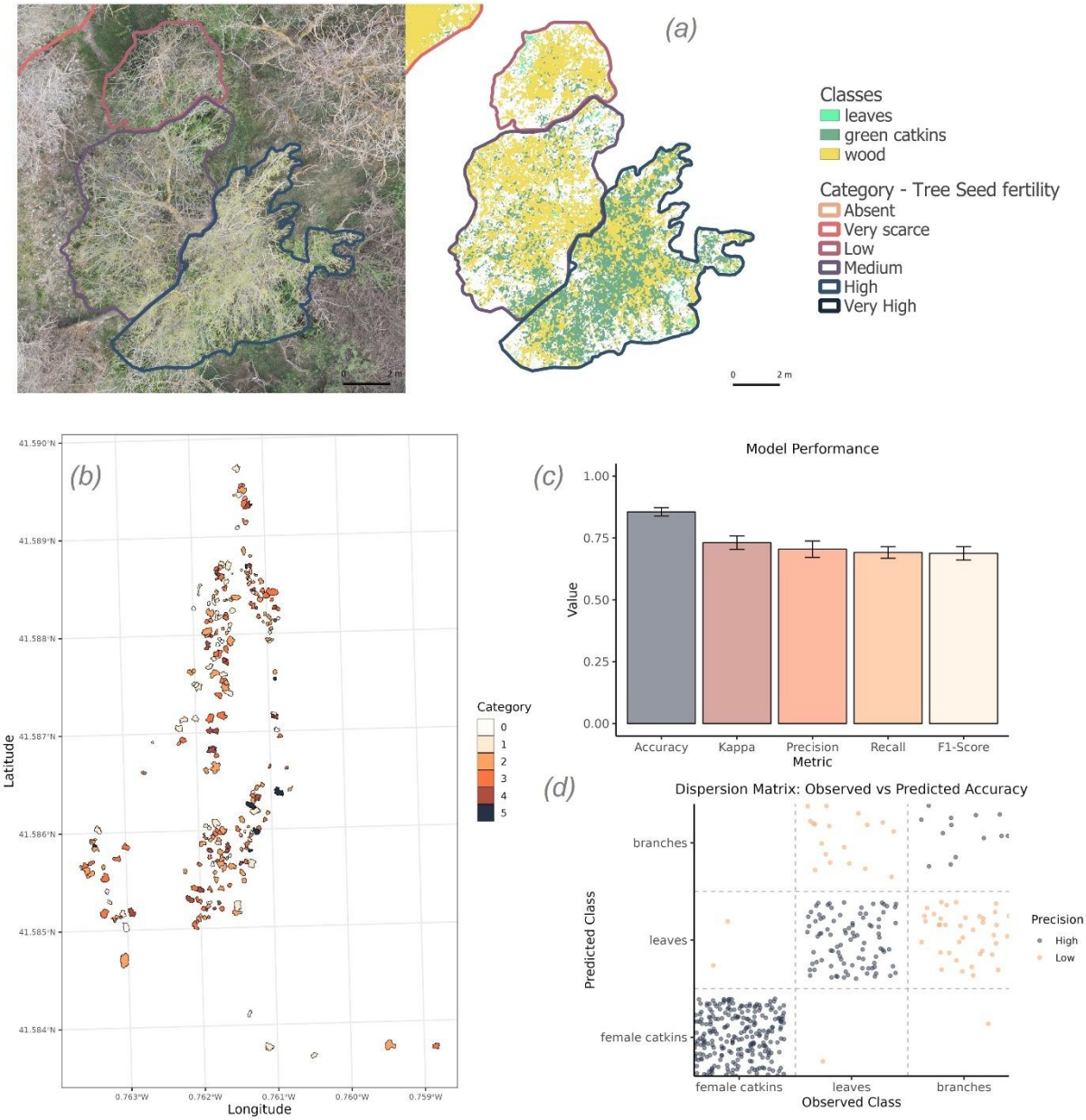

Figure 6. Seed-fertility maps and classifier performance. (a) RGB orthomosaic and corresponding pixel-wise ML classification for the same scene, showing leaves, catkins and wood, and the resulting 0–5 tree-fertility classes at GCU scale. (b) Sampled trees within the GCU, coloured by assigned fertility class. (c) Global performance metrics of the classifier (overall accuracy, Kappa, precision, recall and F1-score). (d) Confusion matrix of observed vs. predicted classes summarising the main error patterns. Together, the panels illustrate the multi-scale product used as a basis for spatial sampling and genetic interpretation.

To illustrate the spatial information provided by the visual scoring route, **Fig. 7** shows the fertility map for *P. sylvestris* in GCU GRB00047. Each symbol corresponds to an RTK-referenced tree crown, with colour encoding the 0–5 fertility category and symbol size proportional to DBH. In this campaign, trees occupy only the lower part of the scale (classes 0–3), in agreement with the fertility distribution described above (**Table 1**). Although it is based on expert annotation, the map reveals a non-random spatial structure: trees with low–medium fertility forms contiguous zones within the stand,

whereas absent/very scarce classes dominate other sectors. DBH values are distributed across fertility classes, indicating that size alone does not explain the observed reproductive pattern.

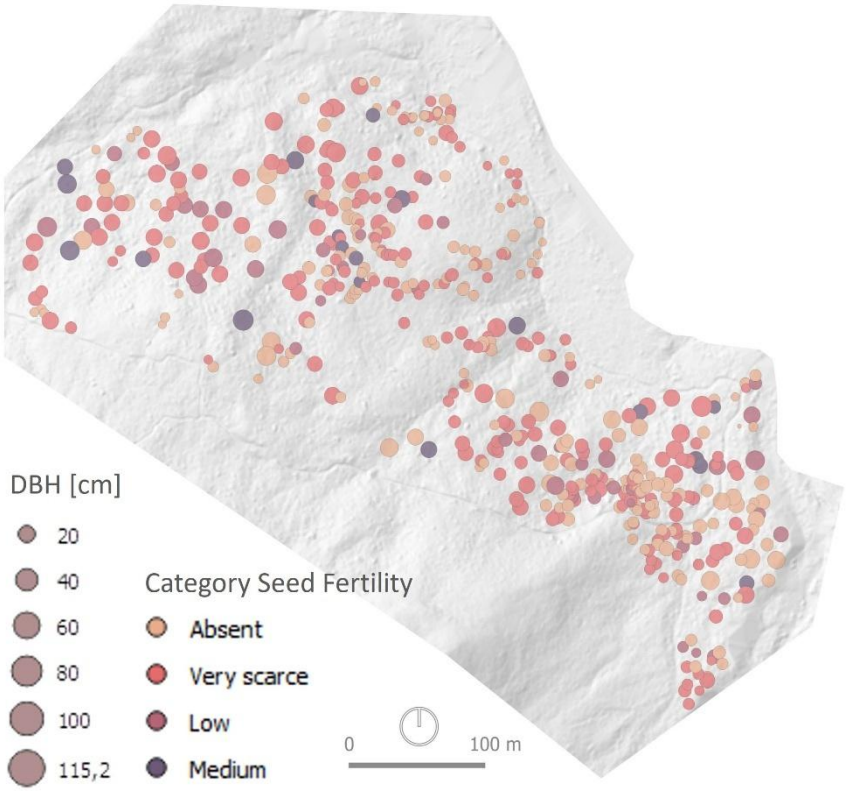

Figure 7. Visual fertility map for *Pinus sylvestris* in GCU GRB00047. Each point represents a georeferenced crown, with point size proportional to DBH and colour indicating fertility class (0–3; no trees reached classes 4–5 in this campaign). The background hillshade shows the local topographic relief.

In species scored by cone counts (*P. sylvestris* and *P. pinaster*), the annotation can explicitly record the position of cones within the crown, so that the 0–5 class is derived from a spatially detailed pattern. In species based on percentage of area (*F. sylvatica* and *P. nigra*), spatial structure is preserved through sectoral recording (N, S, E, W), which stores the fraction of crown area with signal in each direction. In both cases, these crown-level fertility estimates can be related to environmental covariates or used to design spatially explicit genetic sampling.

3.2 Realised fecundity estimated by seedling modelling

We estimated realised fecundity using the genotypes and spatial positions of adults and juveniles of the three remaining species (data for *P. pinaster* are available in D3.5): black poplar (*P. nigra*), beech (*F. sylvatica*) and Scots pine (*P. sylvestris*). For this purpose, we employed the neighborhood model, as implemented in the Bayesian version of NMπ (Chybicki 2018; Chybicki 2023) which simultaneously estimates

individual fecundities, immigration rates, pollen and seed dispersal kernel parameters and selection gradients, allowing to address potential sampling issues. Compared to other available software, NMπ has the additional advantage of being able to handle genomic data from dioecious species, such as black poplar. As black poplar reproduces both sexually and clonally, we preliminary removed clones to avoid overestimating sexual reproduction events and, therefore, realized fecundities. To this specific purpose, we applied the following procedure:

- for clones consisting of adults only, we retained one ramet per genet and used the clone's centroid as a 'synthetic' new spatial position if the average clonal distance was less than 30 meters. Otherwise, we retained all ramets per genet.
- for clones consisting of both adults and juveniles, we retained one adult ramet per genet (applying the same distance criterion) and discarded all juvenile ramets.
- for clones consisting of only juveniles, we retained one ramet per genet and used the clone's centroid as a 'synthetic' new spatial position.

Realised fecundity estimates were based on a subset of 500 unlinked SNP markers selected to have <10% of missing data and a minor allele frequency >0.4 (in plink: --geno 0.1 --maf -0.4 --indep 50 5 2). To ensure that the estimates were not biased by the SNP selection, we repeated the analyses on three different subsets of 500 SNPs each. The results were highly consistent across subsets.

We first used the maximum likelihood (ML) version of NMπ to determine which parameters significantly increased the model's likelihood. We performed model selection following the stepwise procedure described in the NMπ manual and comparing competing models using the likelihood ratio test. After having defined the optimal model, we ran NMπ in its Bayesian version to obtain individual estimates of realised fecundities, together with all the other model parameters (**Table 3**). To guarantee good mixing along the MCMC chain we checked that parameter acceptance rates were between 25 and 45%. We set genotyping error rates to 0.001 for all markers throughout the entire workflow.

Realised effective fecundity showed a highly asymmetrical distribution in each GCU and each species, with only a few trees showing large fecundities significantly different from zero (**Fig. 8-13**). Such an unbalanced contribution to the juvenile generation is extremely common in forest tree populations.

Table 3. Parameters of the neighborhood model obtained with the Bayesian version of NMπ. ms: frequency of seed immigration; s: frequency of self-fertilization; mp: frequency of pollen immigration; ds: mean distance of seed dispersal (expressed in meters); dp: mean distance of pollen dispersal (expressed in meters); bs: shape parameter of seed dispersal; bp: shape parameter of pollen dispersal; ks: intensity of directionality in seed dispersal; kp: intensity of directionality in pollen dispersal; as: prevailing direction of seed dispersal (expressed in π); ap: prevailing direction of seed dispersal (expressed in π).

	Fagus sylvatica		***Pinus sylvestris***		***Populus nigra***	
	FRA00045	SVN00047	FIN00001	GBR00001	AUT00284	ESP00395
ms	0.38	0.12	0.58	0.23	0.25	0.38
s	0.01#	0#	0.01#	0.01#	0#	0#
mp	0.74	0.50	0.77	0.70	0.48	0.54
ds	0#	15.15	39.76	106.58	261.96	50.92
dp	4317.55	33.59	51.00	193.42	868.38	37.67
bs	1#	1#	1#	0.20	0.53	1#
bp	0.05	0.43	1#	1#	0.39	1#
ks	1.71	0.60	1.84	0.63	2.10	1.82
kp	0#	0#	0#	0#	0.77	0#
as	4.94	3.29	1.02	5.12	1.38	5.67
ap	0#	0#	0#	0#	1.18	0#

#parameters were not estimated but fixed at their default value, as their estimation did not improve the likelihood of the final model

For the French GCU of *F. sylvatica*, female and male fecundities ranged from -0.641 to 3.503 and from -0.395 to 3.746, respectively (**Fig. 8**). For the Slovenian GCU of *F. sylvatica*, on the other hand, female and male fecundities ranged from -0.854 to 3.752, and from -0.396 to 3.021, respectively (**Fig. 9**).

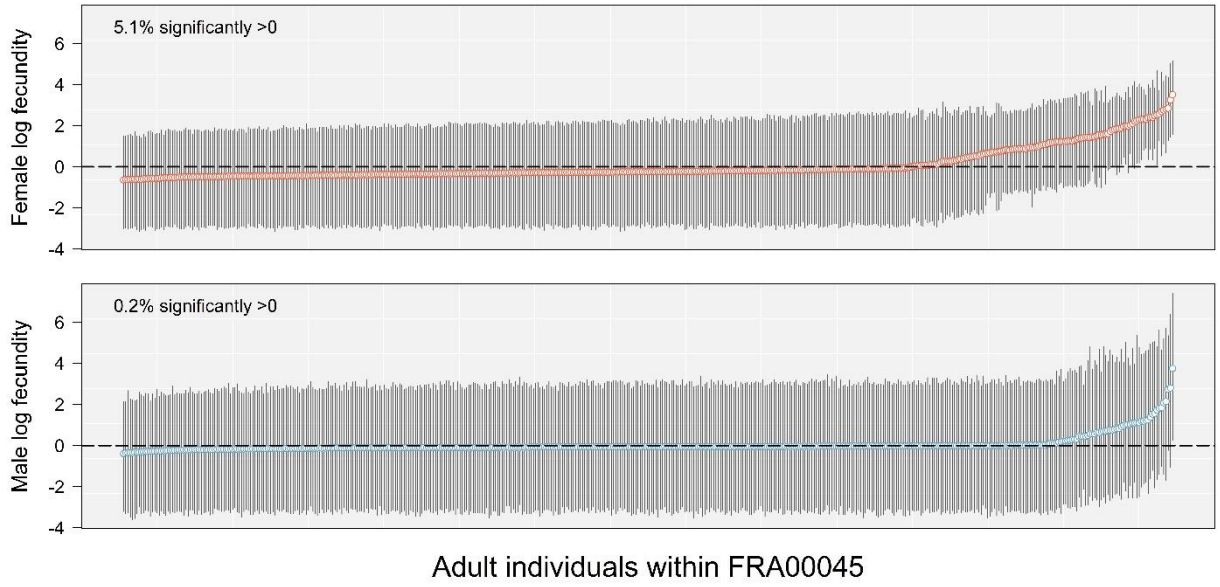

Figure 8. Distribution of female and male individual fecundities in FRA00045

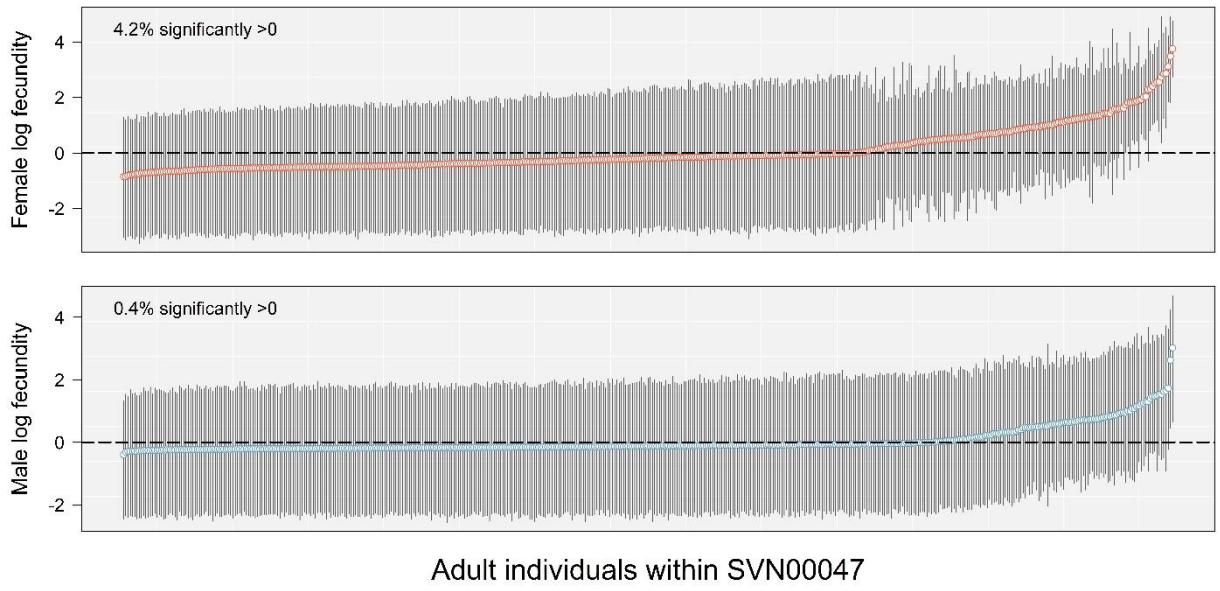

Figure 9. Distribution of female and male individual fecundities in SVN00047

On the one hand, for the Finnish GCU of *P. sylvestris*, female and male fecundities ranged from -0.439 and 1.928, and from -0.019 to 0.098, respectively (**Fig. 10**). For the British GCU of *Fagus sylvatica*, on the other hand, female and male fecundities ranged from -1.458 to 4.597, and from -0.413 to 7.291, respectively (**Fig. 11**).

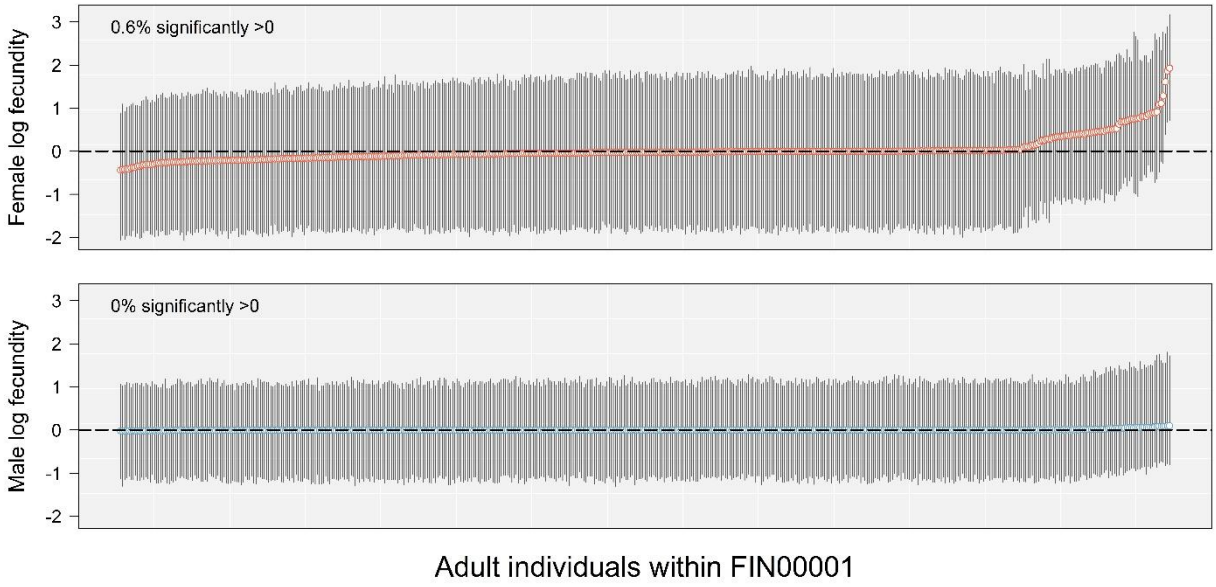

Figure 10. Distribution of female and male individual fecundities in FIN00001

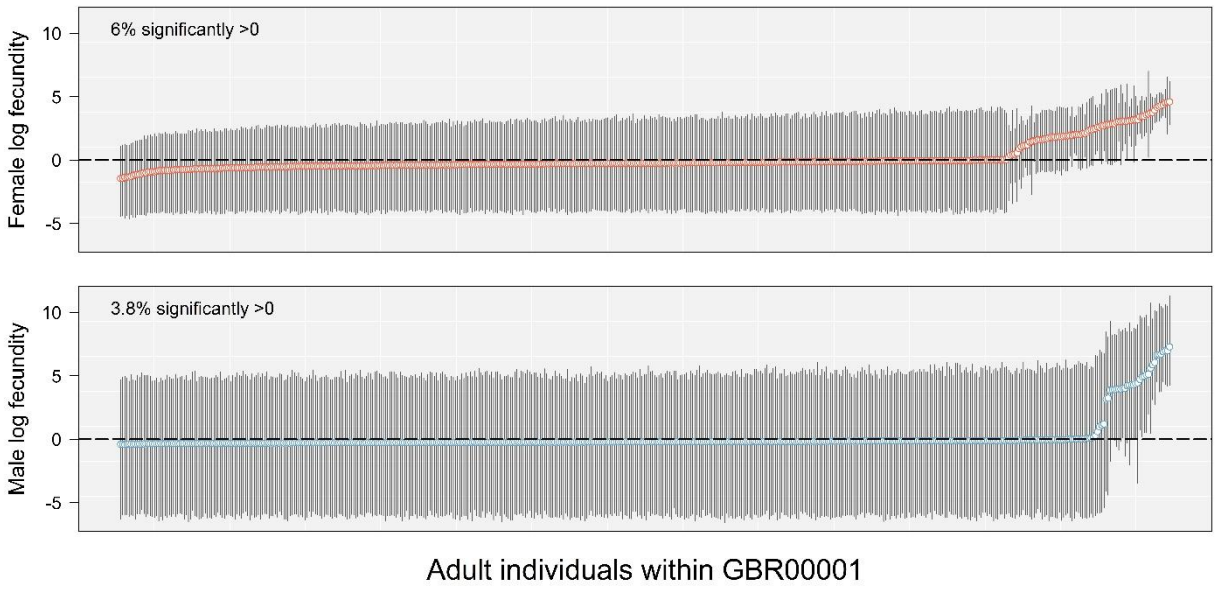

Figure 11. Distribution of female and male individual fecundities in GBR00001

On the one hand, for the Austrian GCU of *P. nigra*, female and male fecundities ranged from -2.074 to 2.401, and from -1.070 to 3.149, respectively (**Fig. 12**). For the Spanish GCU of *P. nigra*, on the other hand, female and male fecundities ranged from -1.199 to 5.395, and from, -0.946 to 2.850, respectively (**Fig. 13**).

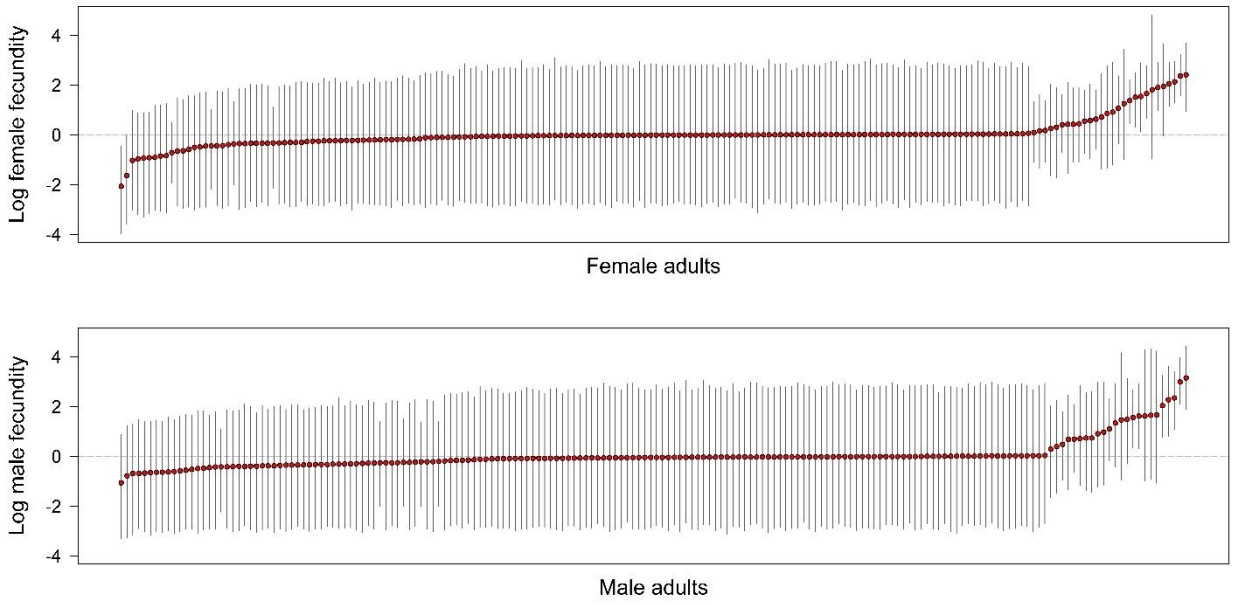

Figure 12. Distribution of female and male individual fecundities in AUT00284

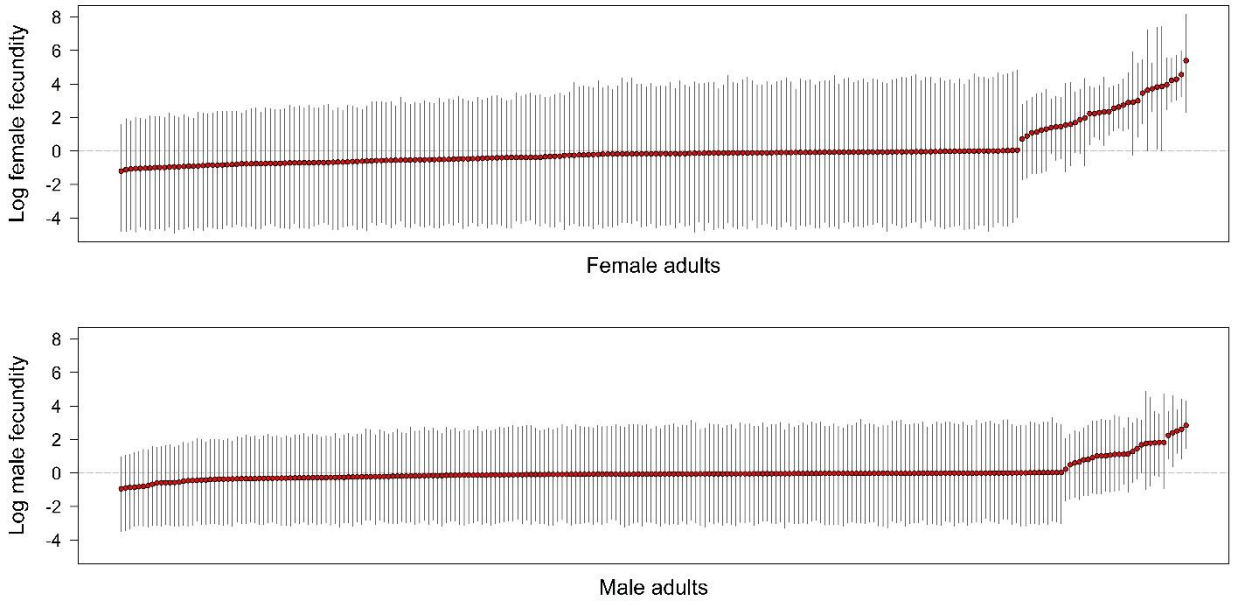

Figure 13. Distribution of female and male individual fecundities in ESP00395

In addition to providing individual fecundity estimates, NMπ returned, for each juvenile, its most likely parentage assignment. In fact, each juvenile can have: 1) both parents in the stands (i.e., parent pair), 2) just one single parent (in this case, we assume it is the mother as seed dispersal is generally more spatially limited), or 3) no local parents. We used parentage assignments to calculate the number of gametes assigned to each adult tree, thus obtaining a further measure of lifetime fitness, which we defined 'reproductive success'. Realised fecundity and individual reproductive success were generally highly correlated (see **Fig. 14** for an example of their relationship).

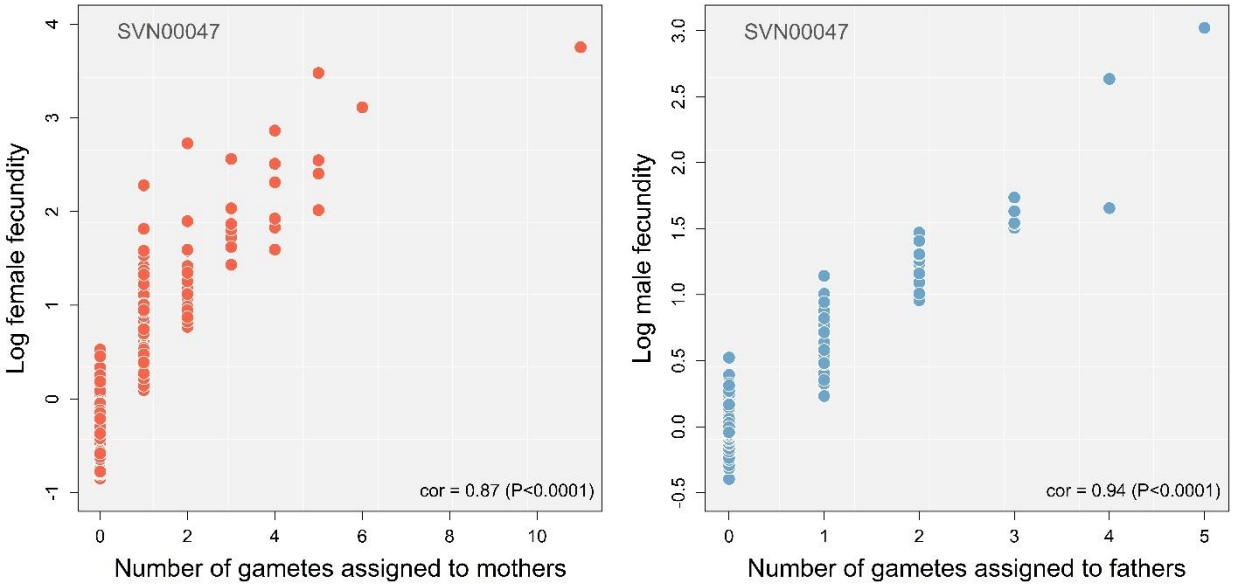

Figure 14. Comparison of individual estimates of reproductive success and realized fecundities, for female (left) and male (right) function, as obtained with NMπ.

The individual estimates of realised fecundity obtained for each GCU and species are available for *a posteriori* statistical modelling of their phenotypic and/or microenvironmental determinants.

3.3 Selection gradients

We have reported about the estimation of selection gradients for black poplar in D3.7, therefore in the present document we will focus only on estimating selection gradients for the other two species. For both Scots pine and beech, we used NMπ to estimate selection gradients. The software implements a Bayesian approach, called the *hierarchical neighborhood model*, which is expressly designed to avoid false positive selection gradients due to the omission of other determinants of reproductive success (Chybicki et al. 2021; Chybicki 2023). For both female and male fecundity, NMπ estimate the posterior distribution of competing regression models, which contain different subsets of phenotypic variables. The model showing the highest posteriors is chosen as the best model and its estimates of selection gradients are shown.

For Scots pine, we tested four selection gradients as potential determinants of realised fecundity, which were: maximum hydraulic conductivity (k_{max}), leaf mass per area (*lma*), specific leaf area (*sla*), and turgor loss point *(tlp*). These variables were obtained as model predictions by using NIRS data, and their pairwise correlations are shown in **Fig. 15**. In the Finnish GCU, no selection gradient was found to have a significant effect on both female and male fecundity. In the British GCU, however, *tlp* was found to have a positive effect on male fecundity, with a regression slope equal to 0.85 (HPD: 0.18–1.58).

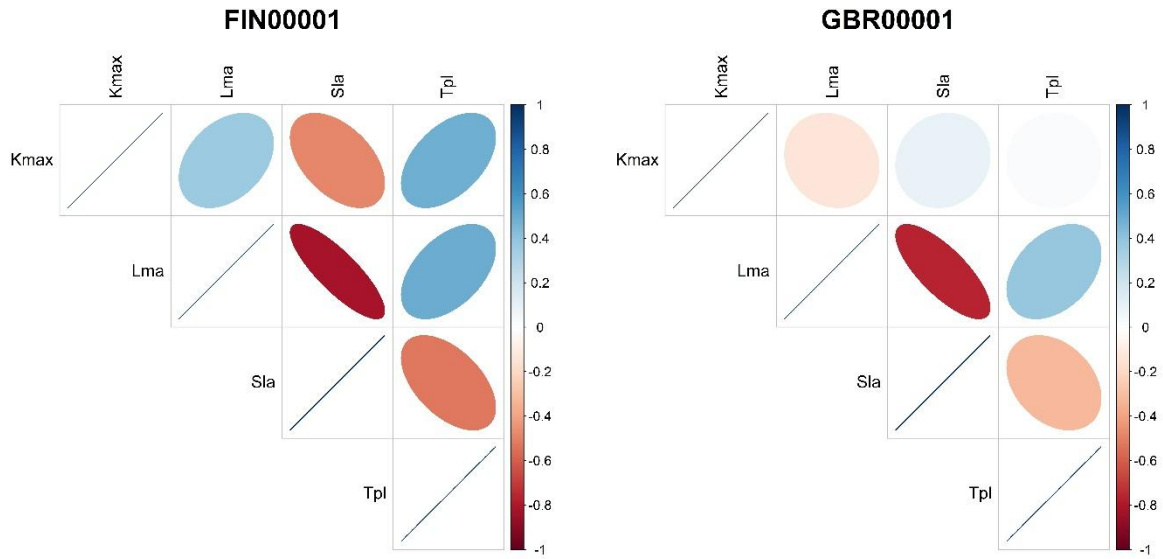

Figure 15. Pairwise correlation between the four selection gradients tested as potential phenotypic determinants of fitness in Scots pine.

For beech, we tested four selection gradients as potential determinants of realized fecundity, which were: capacitance (*cap*), wood density (*density*), water potential at which 50% and 88% of hydraulic conductivity is lost (*P50* and *P88*, respectively). These variables were obtained as model predictions by using NIRS data, and their pairwise correlations are shown in **Fig. 16**. In both the Slovenian and French GCU, no selection gradient was found to have a significant effect on both female and male fecundity.

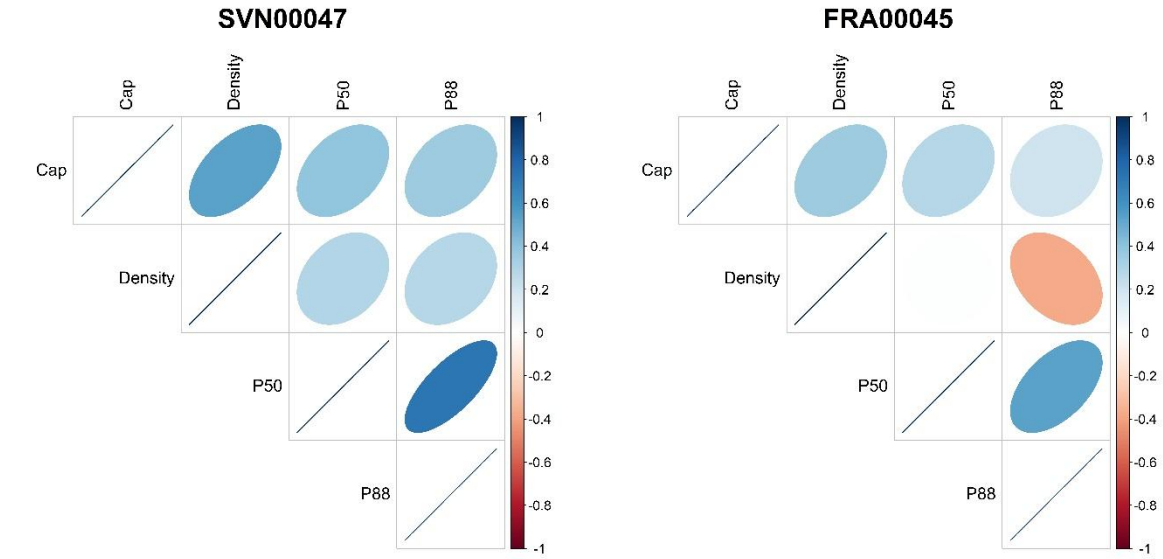

Figure 16. Pairwise correlation between the four selection gradients tested as potential phenotypic determinants of fitness in beech.

4 Conclusions

The combined UAV-based fertility assessment and genetic neighbourhood modelling provide a coherent, multi-scale framework for quantifying fitness components in long-lived forest trees. High-resolution aerial imagery enabled consistent, spatially explicit estimation of canopy-level reproductive output across species and sites, while quality-controlled machine-learning classifications and expert-scored per-tree catalogues ensured robust fertility indices under variable field conditions. These ordinal fertility measures captured strong, ordered gradients in reproductive signal and showed clear relationships with size-normalised seed production.

Genetic analyses complemented these observations by estimating realised fecundity and parentage patterns, revealing the characteristic asymmetry of reproductive contribution within natural stands. The Bayesian neighbourhood model also provided dispersal, mating-system and immigration parameters essential for interpreting demographic processes underlying observed fertility patterns. Parentage-based reproductive success metrics were tightly coupled with realised fecundity, strengthening their utility as fitness proxies.

Trait–fitness analyses using hierarchical neighbourhood models indicated limited but detectable associations between functional traits and fecundity, with evidence for a phenotypic determinant of male fecundity in Scots pine and no detectable selection signals in beech during this campaign. Together, these results establish an integrated approach for linking canopy reproductive expression, effective genetic contribution and potential selective processes. The outputs form a comprehensive basis for subsequent ecological and evolutionary analyses, including the identification of environmental drivers of reproductive variation and the assessment of adaptive potential in the studied populations.

5 Partners involved in the work

Partners involved in this work were UMR, INIA-CSIC, BFW, CNR, INRAE, GIS, Luke, UKCEH, FR.

6 Annexes

Andrew Lyons (2025). uasimg: Drone Images Utilities. R package version 1.9.4. Available at: https://ucanr-igis.github.io/uasimg/

Avanzi, C., Heer, K., Büntgen, U., Labriola, M., Leonardi, S., Opgenoorth, L., ... & Piotti, A. (2020). Individual reproductive success in Norway spruce natural populations depends on growth rate, age and sensitivity to temperature. Heredity, 124(6), 685-698.

Chybicki, I. J. (2018). NMπ—improved re- implementation of NM+, a software for estimating gene dispersal and mating patterns. Molecular Ecology Resources, 18(1), 159-168.

Chybicki, I. J. (2023). NMπ 2.0: software update to minimize the risk of false positives among determinants of reproductive success. Molecular Ecology Resources, 23(5), 1168-1181.

Chybicki, I. J., Oleksa, A., & Dering, M. (2021). Identification of determinants of pollen donor fecundity using the hierarchical neighborhood model. Molecular Ecology Resources, 21(3), 781-800.

Gonzalez-Martinez, S. C., Burczyk, J., Nathan, R. A. N., Nanos, N., Gil, L., & Alia, R. (2006). Effective gene dispersal and female reproductive success in Mediterranean maritime pine (Pinus pinaster Aiton). Molecular Ecology, 15(14), 4577-4588.

Mestre Runge, C., Sekely, J. T., Reudenbach, C., Heer, K., & Opgenoorth, L. (2025). PopNigra - Forgenius (v1.0.0). Zenodo. https://doi.org/10.5281/zenodo.14720409

Meyer, H., & Pebesma, E. (2021). Predicting into unknown space? Estimating the area of applicability of spatial prediction models. Methods in Ecology and Evolution, 12(9), 1620-1633.

Oddou-Muratorio, S. Y. L. V. I. E., & Klein, E. K. (2008). Comparing direct vs. indirect estimates of gene flow within a population of a scattered tree species. Molecular Ecology, 17(11), 2743-2754.

Petit, R. J., & Hampe, A. (2006). Some evolutionary consequences of being a tree. Annu. Rev. Ecol. Evol. Syst., 37(1), 187-214.

Reudenbach, C., Mestre Runge, C., Sekeley, J. T., Heer, K., & Opgenoorth, L. (2025). forgenius-pp (v1.0.0). Zenodo. https://doi.org/10.5281/zenodo.14727432

Tattoni, C., Chianucci, F., Ciolli, M., Ferrara, C., Marchino, L., Zanni, M., ... & Cutini, A. (2021). A comparison of ground-based count methods for quantifying seed production in temperate broadleaved tree species. Annals of Forest Science, 78(1), 11.